# Chapter - 6

# *Photo-Fenton degradation on Mo-doped $NiFe_2O_4$ photocatalyst*

## 6.1 Introduction

The use of antibiotics in humans and animals has increased significantly over the past few decades due to climate change, pollution, and rapid economic development[242]. Tetracycline (TC), a commonly used antibiotic, has been extensively employed in human therapy, veterinary, and agricultural production[243]. Reports indicate that large amount of TC are annually discharged into the aquatic environment with wastewater[244]. Advanced oxidation processes (AOPs) utilizing highly reactive free radicals are effective and promising methods for mitigating environmental risks by degrading antibiotics like TC.[245] The conventional homogeneous Fenton process involves mixing a $Fe^{2+}$ solution with $H_2O_2$ to produce ·OH ($Eq$: $Fe^{2+} + H_2O_2 \rightarrow Fe^{3+} + \cdot OH + OH^-$).[246] The regeneration of $Fe^{2+}$ from $Fe^{3+}$ is a critical issue because the ($Eq$: $Fe^{3+} + H_2O_2 \rightarrow Fe^{2+} + \cdot OOH + H^+$) back reaction is much slower than the forward reaction.[246] Issues like the requirement of a low (working) pH range (around 2 to 3) and high production of iron sludge residue due to limited $Fe^{2+}$ regeneration seriously hinder the practical application of the homogeneous Fenton technique.[247]

In contrast, the photo-driven heterogeneous Fenton reaction, relying on efficient hydroxyl radicals (·OH) production from $H_2O_2$, is a green method favoured for chemically degrading a wide range of non-biodegradable pollutants to their non-toxic fragments in the presence of iron-based photocatalysts.[248] Light of suitable wavelength photo-excites the semiconductor photocatalyst. The photo-excited electrons in the photocatalyst's conduction band (CB) reduce $H_2O_2$ to produce ·OH radicals, while oxidation occurs at the holes in the valence band (VB).[249] The separate oxidation and reduction sites in photo-Fenton photocatalysts enhance efficiency by overcoming the rate-limiting issues of conventional Fenton processes. Moreover, the process offers high catalytic efficiency, facilitated by the

robust regeneration of $Fe^{2+}$ by photoexcited electrons ($Fe^{2+} \rightleftharpoons Fe^{3+}$), ensuring continuous redox cycling. Additionally, it demonstrates broader pH tolerance, with simple operational requirements, mild reaction conditions, and overall higher efficiency.

The spinel superparamagnetic $NiFe_2O_4$ semiconductor is a prospective candidate for the photo-Fenton degradation of organic pollutants due to its moderate visible light band gap (1.9-2.2 eV) and good photochemical stability.[89] Nonetheless, pristine $NiFe_2O_4$ characteristically exhibits low surface reaction rates, rapid recombination of photogenerated electrons and holes, and poor visible light absorption.[250] Various strategies have been employed to address these shortcomings and enhance its catalytic efficiency. A promising approach is metal ion doping to alter the physical and chemical properties of spinel $NiFe_2O_4$. Typically, the dopant level introduced in the band gap enhances charge separation and slows the recombination process. There are a few instances of the metal-doped $NiFe_2O_4$ photocatalysis. Thus, Alzahrani et al. reported the synthesis of Nd-doped $NiFe_2O_4$ and Gd-doped $NiFe_2O_4$ photocatalysts for photocatalytic degradation of organic effluents. They observed the superior photocatalytic activity of doped $NiFe_2O_4$ samples than bare $NiFe_2O_4$ due to reduction in the recombination of electrons and holes.[251,252] Similarly, enhancement in the photocatalytic activity of Co-doped $NiFe_2O_4$ and Mg-doped $NiFe_2O_4$ were ascribed to dopant energy states slowing the recombination of electrons and holes.[253,254]

In this regard, Molybdenum (Mo) is a particularly suitable dopant, as it can modify the electronic properties (carrier concentration or CB position) and reduce the recombination of photogenerated charge carriers. Mo exists in multiple oxidation states (+4, +5, and +6) and the dopant energy level in the $NiFe_2O_4$ band gap can improve the iron cycle ( $Fe^{2+} \rightleftharpoons Fe^{3+}$) in Fenton catalysis, enhancing catalytic efficiency. For instance, Ying et al. found that the $TiO_2$ doped by $Mo^{6+}$ extends the absorption edge and decreases

the interfacial charge transfer resistance. The photocatalytic activity of Mo-doped $TiO_2$ was much better than pure $TiO_2$.[255] Likewise, in a recent report, authors have shown that Mo-doped $FeS_2$ demonstrates improved stability and photo-Fenton activity.[256] Considering the advantages mentioned and the variable oxidation states of Mo, which are crucial for the Fenton reaction, this study explores the photo-Fenton activity of Mo-doped $NiFe_2O_4$. Notably, there has been no investigation into the design and effects of Mo-doping in spinel $NiFe_2O_4$ on its photo-Fenton TC degradation activity, making this investigation a novel contribution to the field.

Previous studies[47,80,219], combining experimental and computational approaches, indicate that for a photo-Fenton catalyst to be effective, its photo-excited CB must interact favorably with $H_2O_2$ to facilitate ·OH radical production. Guided by this principle, the present Chapter employed Density functional theory (DFT) and time-dependent DFT (TD-DFT) calculations to qualitatively evaluate whether the Mo-doped $NiFe_2O_4$ satisfies this criterion prior to experimental investigations. The following description highlights the novelty of this research work. There is no previous investigation on the photo-Fenton properties of Mo-doped $NiFe_2O_4$. The Mo-dopant can act as a donor dopant level and a shallow trap in the $NiFe_2O_4$ band gap to prevent photoexcited electron-hole recombination, improve charge separation, and extend carrier lifetimes. Moreover, favorable $Mo^{6+}/Mo^{5+}$ redox potential also implies the possibility of increased $Fe^{3+}$ to $Fe^{2+}$ back reaction rate. Critically, DFT and TD-DFT calculations were used to predict that Mo doping would result in charge redistribution, alter electronic transitions, and facilitate efficient hydroxyl radical generation through enhanced $H_2O_2$ activation. Hence, such doping can substantially improve the photocatalytic activity of Mo-doped $NiFe_2O_4$. The improved activity and the superparamagnetic properties of the doped $NiFe_2O_4$ nanoparticles (enabling easy recovery

and dispersal of the nanoparticles for reuse) could result in an industrially attractive photocatalyst.

Satisfied by the DFT calculation results and the possibility of enhanced photocatalytic activity of this novel doped nanomaterial, this Chapter investigates the photo-Fenton properties of Mo-doped $NiFe_2O_4$ nanoparticles. The latter are the same nanoparticle samples prepared earlier in Chapter 5. In Chapter 5, only the organic pollutant co-adsorption properties of $NiFe_2O_4$ and Mo-doped $NiFe_2O_4$ particles were investigated. Comprehensive materials characterizations of these nanomaterials investigating physicochemical properties, microstructure, and chemical composition have already been presented and discussed in Chapter 5. The optical band gap, Mott-Schottky (MS), and Electrochemical impedance spectroscopy (EIS) investigations of $NiFe_2O_4$ and Mo-doped $NiFe_2O_4$ nanomaterials have been discussed in the present Chapter. MS and EIS characterizations have been used to determine the flat band potential, semiconductor type, and charge transfer resistance of the nanomaterials. The effects of Mo-dopant amount, $H_2O_2$ concentration, and pH on photo-Fenton TC degradation were systematically investigated. Under visible light irradiation, the synthesized Mo-doped $NiFe_2O_4$ nanoparticles demonstrated enhanced photo-Fenton degradation of tetracycline. Scavenger experiments identified the key reactive species responsible for the photocatalytic activity. Experimental and DFT calculation results were combined to understand the photocatalytic mechanism in this photo-Fenton process.

## 6.2 Experimental section

### 6.2.1 Materials used for experimental procedures

AR grade precursor materials $Ni(NO_3)_2.6H_2O$ (Merck), $Fe(NO_3)_3.9H_2O$ (Merck), $(NH_4)_6Mo_7O_{24}.4H_2O$ (Merck), NaOH (Merck), $H_2O_2$ (Qualigens), tetracycline (Merck), Isopropyl alcohol (Merck), $AgNO_3$ (Merck), and triethanolamine (Qualigens) were used for

experimental procedures without extra purification. Double distilled water (DW) was used as a solvent for all the experiments in this research.

### 6.2.2 Hydrothermal synthesis of Mo-doped $NiFe_2O_4$ nanoparticles

Pure and Mo-doped $NiFe_2O_4$ samples with various atomic percentages (at. %) of Mo doping were synthesized by hydrothermal method. A detailed synthesis procedure is discussed in Chapter 5.

### 6.2.3 Control experiments on catalytic/photocatalytic activity of the nanocomposites

The 1MNIF sample was first tested for Fenton activity toward tetracycline (TC) degradation in the dark. In another control experiment, the 1MNIF sample was also tested for TC degradation activity in an aqueous medium under visible light irradiation (but without $H_2O_2$). Little or negligible TC degradation was observed under these reaction conditions.

### 6.2.4 Photo-Fenton catalytic activity

The photo-Fenton activities of the synthesized catalysts (undoped $NiFe_2O_4$, 1MNIF, 2MNIF, and 4MNIF) were examined for TC degradation under cool white 14W LED light (intensity: 1430 $W/m^2$) irradiation. A 1 mg/ml dispersion of photocatalyst nanoparticles was prepared by introducing the required amount of nanoparticles in the specified volume of double distilled water and bath sonicating for 20 minutes. In each experiment, 3ml of 10 ppm TC aqueous solution with 100 µL of earlier prepared photocatalyst suspension was taken in a 3.5 ml quartz cuvette having 1cm path length. The resulting mixture was kept in the dark for 30 minutes until the establishment of the adsorption-desorption equilibrium. An adequate amount of $H_2O_2$ was then added to the mixture. This reaction mixture was then exposed to visible light. The absorption spectrum of the TC solution was recorded at

regular intervals after separating the photocatalyst with a magnet. The absorbance was measured at 358 nm, the characteristic absorption peak of TC. As TC degradation progresses, the intensity of the characteristic absorption peak diminishes.

Several control experiments were carried out under various conditions. For instance, experiments were conducted at different pH values to determine the optimal reaction pH. The effect of $H_2O_2$ dosage on the photo-Fenton activity was also investigated by evaluating the photo-Fenton activity of the Mo-doped $NiFe_2O_4$ sample at various $H_2O_2$ concentrations in the reaction mixture. Finally, the best photocatalyst with the highest photo-Fenton activity among the Mo-doped $NiFe_2O_4$ samples was assessed under optimal pH and $H_2O_2$ conditions.

Separate scavenger experiments were conducted to investigate OH· radical, photogenerated electrons/holes, and superoxide anion radical generation in the photo-Fenton degradation process. Isopropyl alcohol (IPA), $AgNO_3$, and triethanolamine (TEOA) were used to capture OH·, electrons, and holes, respectively. For the active species determination experiment, 100µL of 0.185 mM IPA or 20µL of 0.5 M TEOA, or 10µL of 0.82 mM $AgNO_3$ were added to the reaction mixture. The rest of the experiment remained the same. On the other hand, the nitro blue tetrazolium (NBT) test detected the superoxide radical anion formation ($O_2^{\cdot-}$). All the photo Fenton degradation experiments were conducted at ~27°C temperature. The degradation efficiency (%) of each photocatalyst was calculated by equation 6.1,

$$Degradation\ efficiency\ (\%) = \frac{(C_0 - C_e)*100}{C_0} \qquad (6.1)$$

In Eq. 6.1, $C_0$ and $C_e$ represent the initial and equilibrium concentrations of TC in the reaction mixture (mg $L^{-1}$).

### 6.2.5 DFT calculations

The location of Mo dopant in the $NiFe_2O_4$ lattice was determined by plane-wave DFT calculations in previous chapter 5. The optimized Mo-doped $NiFe_2O_4$ model with the most negative formation energy was utilized for further processing. A cluster of Mo-doped $NiFe_2O_4$ was built from this model using the MAPS 4.4.1 software (released by Scienomics).[143] As in Chapter 5, this Mo-doped $NiFe_2O_4$ cluster model is denoted by the abbreviation 'MoNIF33' cluster throughout the present Chapter.

The $H_2O_2$ molecule was built using GaussView 6.0 software in the next step. This molecule was optimized using the DGDZVP basis set with the B3LYP (Becke-3-Parameter-Lee-Yang-Parr) functional in the Gaussian 16 software. DFT calculations were conducted to investigate the interaction of $H_2O_2$ with the MoNIF33 cluster in the ground state. All DFT calculations were performed at the same level of theory as discussed earlier. Natural bond orbital (NBO) analysis gave the charge transfer/ delocalization due to the $H_2O_2$-MoNIF33 interaction. All calculations were performed in the gas phase.

### 6.2.6 TD-DFT calculations

Excited state TDDFT calculations at the same level of theory as the ground state calculations gave the gas phase UV-visible spectrum of the MoNIF33 cluster. The HOMO and LUMO locations in the cluster corresponding to the most intense excitation frequency were calculated. Separate TDDFT calculations (gas phase) were carried out to investigate the interaction of $H_2O_2$ with the excited state HOMO location of the MoNIF33 cluster.

## 6.3 Results and Discussion

### 6.3.1 Material characterization

The samples prepared for this study were characterized using various techniques, including X-ray diffraction (XRD), scanning electron microscopy (SEM), X-ray photoelectron spectroscopy (XPS), vibrating sample magnetometry (VSM), and high-resolution transmission electron microscopy (HRTEM). A detailed discussion of these characterizations for both pure $NiFe_2O_4$ and Mo-doped $NiFe_2O_4$ is provided in Chapter 5. Furthermore, additional techniques such as ultraviolet-visible diffuse reflectance spectroscopy (UV-DRS), electrochemical impedance spectroscopy (EIS), and Mott-Schottky analysis were employed to investigate the photocatalytic properties of the pure and doped $NiFe_2O_4$. These findings are discussed in detail in the current chapter.

Figure 6.1 (a-d) shows the band gap determination of pure $NiFe_2O_4$ and different Mo-doped $NiFe_2O_4$ samples, calculated by the Tauc equation. The graph was plotted between $(\alpha h\nu)^{1/n}$ versus photon energy ($h\nu$) to determine the band gap. The symbols $\alpha$, $h$, and $\upsilon$ are the absorption coefficient, Planck's constant, and photon's frequency in the Tauc relation. For direct transition, n equals 1/2, and 2 for indirect transitions.[205] The band gap ($E_g$) decreases from 2.014 ($NiFe_2O_4$) to 1.939 eV (2MNIF) after Mo-doping. The band gap of Mo-doped $NiFe_2O_4$ initially decreases and then increases with increasing Mo doping percentage after 2MNIF.

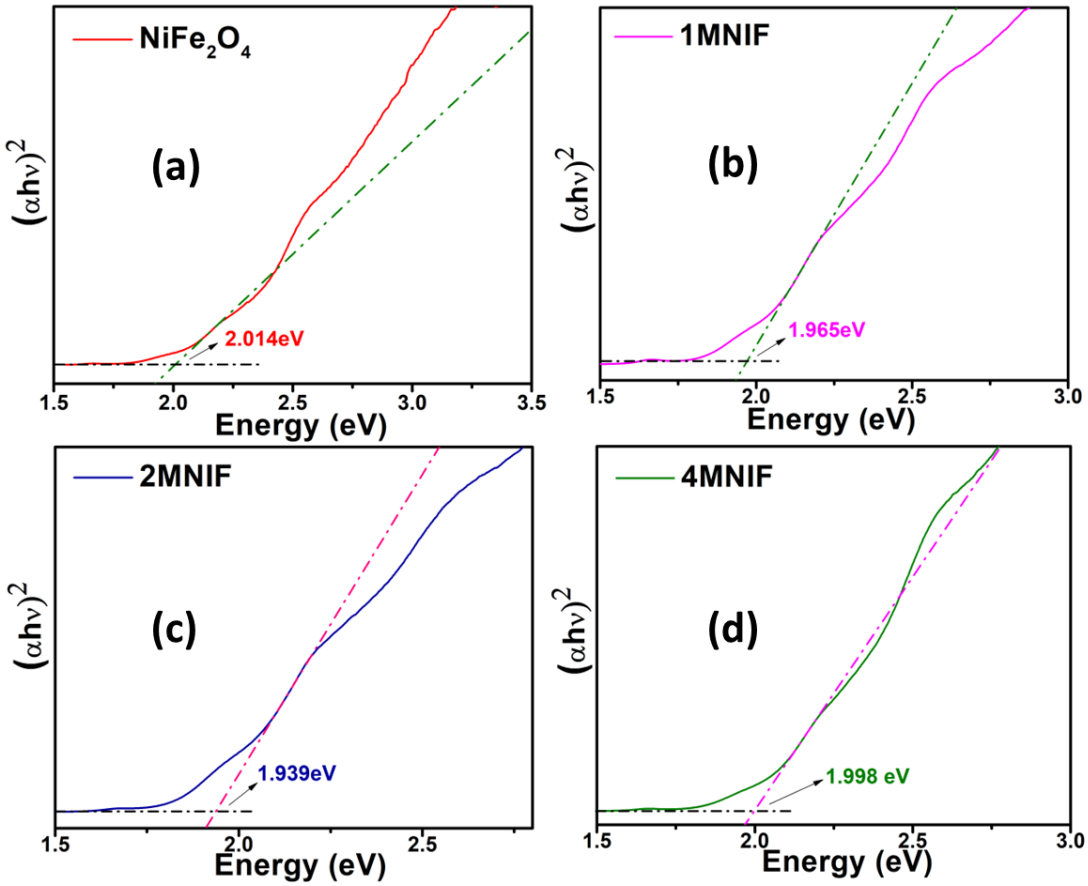


**Figure 6.1** Tauc plots for (a) pure $NiFe_2O_4$, (b)1MNIF, (c) 2MNIF, and (d) 4MNIF samples.

Electrochemical impedance spectroscopy (EIS) observations are related to the kinetics of charge carriers' recombination. Figures 6.2a and 6.2b show the Nyquist plot of pure $NiFe_2O_4$, 1MNIF, 2MNIF, and 4MNIF samples. The diameter of the semicircle of the Nyquist plot is directly proportional to the charge transfer resistance and inversely proportional to charge separation.[257]. Among all samples, the Nyquist plot of 1MNIF had the least semicircle diameter, indicating the best charge separation during the reaction.

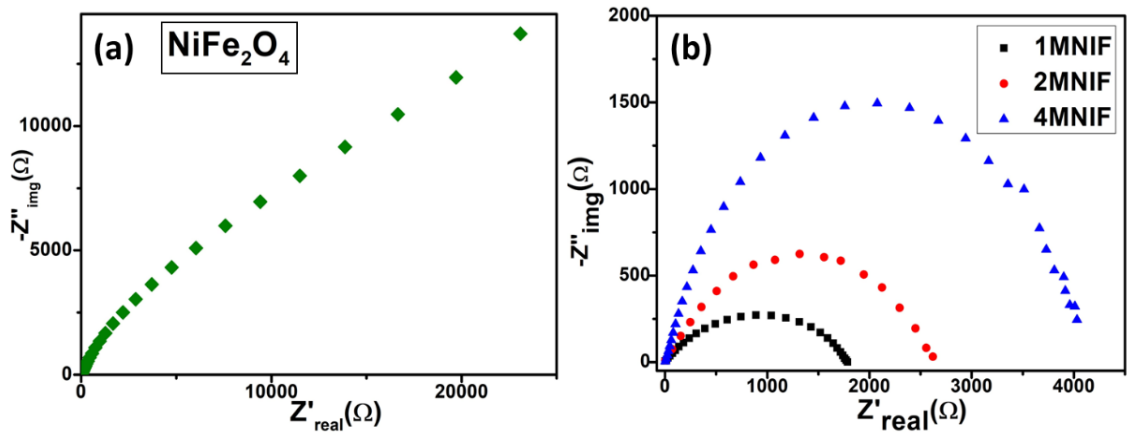


**Figure 6.2** Nyquist plots of (a) pure $NiFe_2O_4$ and (b) Mo-doped $NiFe_2O_4$ samples.

Mott Schottky (MS) data were acquired at 500 Hz to ascertain the semiconductor type and calculate the band edge positions of $NiFe_2O_4$ and 1MNIF semiconductors. The equation V(NHE) = V(Ag/AgCl) + 0.059 pH + 0.197 was used to convert the potential (V) to the normal hydrogen electrode (NHE) scale for the MS plots.[258] The pH of the electrolyte was approximately 6.8. Figures 6.3a and 6.3b illustrate the MS plot of the pure $NiFe_2O_4$ and 1MNIF particles. Their MS plots show a positive slope, so pure $NiFe_2O_4$ and 1MNIF are n-type semiconductors. The pure $NiFe_2O_4$ and 1MNIF have CB edge potentials of -0.71 and -0.43 V, respectively. Equation $E_g = E_{VB} - E_{CB}$ was utilized to determine the VB edges of pure $NiFe_2O_4$ and 1MNIF using these CB edge values. The calculated VB edge is 1.31 V for pure $NiFe_2O_4$ and 1.535 V for the 1MNIF sample.

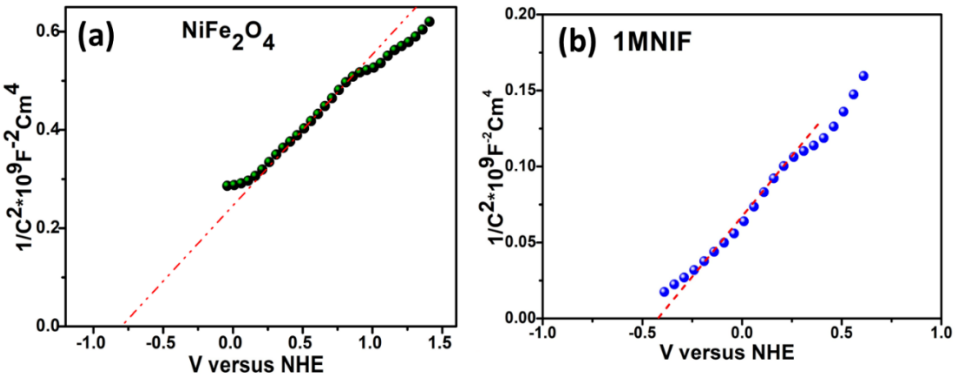


**Figure 6.3** Mott-Schottky plots for (a) pure $NiFe_2O_4$ and (b) 1MNIF photocatalyst.

### 6.3.2 Photo-Fenton activity

Figure 6.4a shows that the dark Fenton TC degradation on 1MNIF at pH~3 was approximately ~18% in a 90-minute reaction time. Another control experiment was conducted under visible light irradiation using the 1MNIF sample without the external addition of $H_2O_2$. Only ~8% TC degradation was observed (Fig 6.4b) during this control experiment.

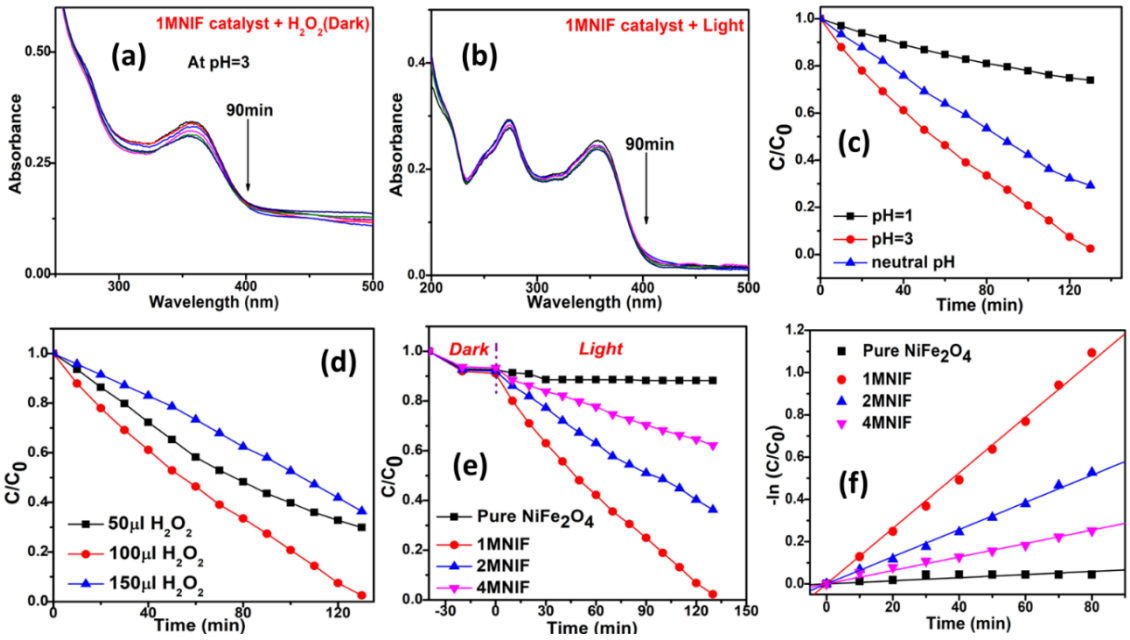


**Figure 6.4** The UV visible spectra of tetracycline degradation in, (a) 1MNIF catalyst + $H_2O_2$ (dark), (b) 1MNIF catalyst + Light system, (c) Effect of pH on photo-Fenton degradation of TC on 1MINF catalyst, (d) Effect of $H_2O_2$ amount on photo-Fenton degradation of TC on 1MNIF catalyst at pH 3, (d) Comparison plot of photo-Fenton TC degradation activity of pure $NiFe_2O_4$, 1MNIF, 2MNIF, and 4MNIF, and (e) Linear plot of pseudo-first order kinetics of pure $NiFe_2O_4$, 1MNIF, 2MNIF, and 4MNIF photocatalyst.

The photo-Fenton activities of Mo-doped and undoped $NiFe_2O_4$ for TC degradation have been investigated. Photo Fenton activities of the 1MNIF doped sample were studied at pH ~ 1, 3, and 6 (near neutral). Figure 6.4c shows that the best photo Fenton activity of

1MNIF was observed at pH 3. Another set of experiments was conducted to optimize the $H_2O_2$ amount in the photocatalysis reaction mixture at pH 3 (Figure 6.4d). The volumes of $H_2O_2$ used in the experiments were 50µl, 100µl, and 150µl of 0.5M $H_2O_2$. The best photo-Fenton activity on the 1MNIF sample was obtained with 100µl of $H_2O_2$. Nearly, ~99% of photo-Fenton degradation of TC by 1MNIF was completed in 130 min (Figure 6.4d). In contrast, only 60 % of TC degradation was observed when 150µl of 0.5M $H_2O_2$ was used. The reduction in TC degradation occurred because excess (unreacted) $H_2O_2$ acts as a hydroxyl radical (·OH) scavenger and generates hydroperoxyl radical (•HO2) (shown in equations 6.2 and 6.3).[259] This $•HO_2$ radical is a considerably weaker oxidizing agent than ·OH radical.[259]

$$H_2O_2 + {}^{\bullet}OH \rightarrow •HO_2 + H_2O \qquad (6.2)$$

$$^{\bullet}OH + •HO_2 \rightarrow H_2O + O_2 \qquad (6.3)$$

Figure 6.4e displays the concentration versus time plots of TC degradation under optimum photo Fenton conditions on different Mo-doped and undoped $NiFe_2O_4$ samples. Among all photocatalysts, 1MNIF shows the best TC degradation photo-Fenton activity, and the undoped $NiFe_2O_4$ sample shows poor photo-Fenton activity. Figure 6.4f shows that the TC degradation concentration versus time data fits best pseudo-first-order kinetics ($0.988<R^2<0.999$). Table 6.1 compares the photo-Fenton activity of our photocatalyst for tetracycline degradation with previously published research work. The activity of the Mo-doped $NiFe_2O_4$ is among the best reported in the literature for doped semiconductors. Figure 6.5a shows the UV-visible absorbance spectra of photo-Fenton degradation of TC by 1MNIF photocatalyst at pH 3. Within 130 min, ~99% of TC was degraded under visible light irradiation.

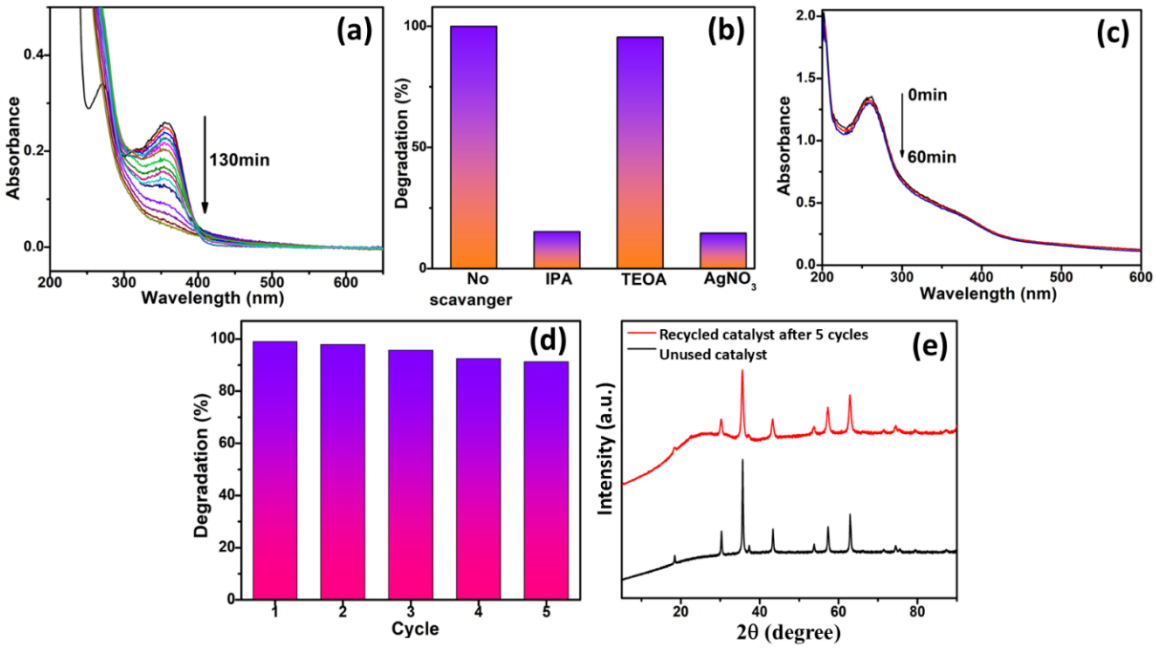


**Figure 6.5** (a) UV-visible spectra of TC degradation by 1MNIF photocatalyst, (b) bar chart presenting the scavenger test results, (c) NBT test for TC degradation, (d) Recyclability test of 1MNIF composite, and (e) XRD patterns of unused and recycled catalyst (1MNIF) after 5 cycles. (Reaction conditions for UV-Visible measurements- Concentration of TC- 10ppm, pH-3, $H_2O_2$ added- 100µl of 0.5M, and optical path- 10mm)

**Table 6.1** Comparison of TOF of various photocatalysts obtained from literature survey.

| Catalyst | Working Conditions | Degradation efficiency | TOF (µmol $g^{-1}$ $h^{-1}$) | $H_2O_2$ normalized TOF ($10^{-6}$ $mg^{-1}$ $h^{-1}$ L) | References |
|---|---|---|---|---|---|
| 1MNIF | TC- 10mg/L, Catalyst- 0.1mg in 3ml of TC solution, Time- 130 min, Light source- Cool white LED, $H_2O_2$-16.13 mM | 99.50% | 309.99 1 µmol $g^{-1}$ $h^{-1}$ | 19.22 | This work |

| | | | | | |
|---|---|---|---|---|---|
| Surface oxygen vacancy and carbon dopant co-decorated $ZnFe_2O_4$ | TCH* - 100ml of 20mg/L, Catalyst- 0.5g/L, Time- 50 min, Light Source- Xenon lamp (300W), $H_2O_2$-10 mM | 90.8% | 90.63 μmol $g^{-1}$ $h^{-1}$ | 9.06 | [260] |
| Hollow Fe doped $In_2O_3$ | TC- 50ml of 20mg/L, Catalyst- 0.4g/L, Time- 60 min, Light source- Xenon lamp (300W), $H_2O_2$-10mM | 100% | 112.50 μmol $g^{-1}$ $h^{-1}$ | 11.25 | [261] |
| 3D hierarchical Fe doped $Bi_4O_5I_2$ | TC- 40ml of 20mg/L, Catalyst- 0.75g/L, Time- 80 min, light source- Xenon lamp (500W), $H_2O_2$-17.4 mM | 94% | 42.30 μmol $g^{-1}$ $h^{-1}$ | 2.43 | [262] |
| Bi and Cu doped $LaFeO_3$ | TC-100ml of 40mg/L, Catalyst- 1.0 g/L, Time- 60 min, Light source- 70W Phillips light, $H_2O_2$ - 49 mM | 94.6% | 85.14 μmol $g^{-1}$ $h^{-1}$ | 1.74 | [263] |
| Ni doped $BiFeO_3$ | TC- 50ml of 10mg/L, Catalyst - 0.7g/L, Time- 120 min, Light source- 500W xenon lamp, $H_2O_2$- 4 mM | 96% | 15.43 μmol $g^{-1}$ $h^{-1}$ | 3.86 | [264] |

| | | | | | |
|---|---|---|---|---|---|
| Fe and Ti co-doped g-$c_3n_4$ | OxyTC**-100ml of 10g/L, Catalyst-0.1g/L, Time-60 min, Light source- 300W xenon lamp, $H_2O_2$ - 20mM | 98% | 212.84 μmol $g^{-1}$ $h^{-1}$ | 10.64 | [265] |

*TCH means Tetracycline hydrochloride, **OxyTC means oxytetracycline.

Separate active species trapping tests were conducted with IPA, $AgNO_3$, and TEOA. IPA is a hydroxyl radical scavenger, $AgNO_3$ is an electron scavenger, and TEOA serves as a hole scavenger.[266] The photo-Fenton reaction on the 1MNIF catalyst almost completely degraded tetracycline in 130 min without any scavenging agent. In comparison, the photo-Fenton TC degradation efficiencies on the 1MNIF sample with either IPA, or $AgNO_3$, or TEOA were ~15.9%, ~14.6%, and 95.5% (Figure 6.5b), respectively. This demonstrates that hydroxyl radicals and photogenerated electrons are the predominant active species for photo Fenton TC degradation on the 1MNIF sample.

In addition to the above, the Nitro blue tetrazolium (NBT) test was used to detect the existence of superoxide radicals in the aqueous solution of 1MNIF photocatalyst.[267] Following the standard procedure, 3 ml of a $2.5 \times 10^{-2}$ mM NBT solution was placed in a quartz cuvette, and 100 microliters of the dispersed photocatalyst nanoparticles (1 mg/ml) were added under (cool white LED) visible light irradiation. The supernatant was examined by UV-visible absorbance spectroscopy after the photocatalyst was separated using a magnet after fixed time intervals (Figure 6.5c). No change in the NBT molecule's absorption maximum at ~265 nm with time confirms that the superoxide radical ($\bullet O^{2-}$) generation is negligible and is not an active species in TC degradation.

The recyclability test of 1MNIF was conducted for five consecutive cycles of photo-Fenton degradation of TC. The following procedure was used for the catalyst recyclability experiments. Initially, 6 mg of the 1MNIF catalyst was added to 30 mL of a

10 ppm TC solution at pH 3 and subjected to sonication. The mixture was then kept in the dark for 30 minutes to establish adsorption-desorption equilibrium. Subsequently, an appropriate amount of 0.5 M $H_2O_2$ was added to the reaction mixture, which was then exposed to visible light from a cool white LED source. After each cycle, the catalyst was magnetically separated, thoroughly washed with distilled water, and dried in a hot air oven. Figure 6.5d illustrates the reusability of 1MNIF via consecutive experiments (5 cycles). The photo-Fenton activity of 1MNIF was ~91.5% after 5 cycles. Figure 6.5e compares the XRD patterns of fresh and recycled 1MNIF samples. All XRD peaks of recycled 1MNIF match those of the unused fresh 1MNIF sample. The 1MNIF photocatalyst shows good photostability after five photocatalytic cycles.

The leaching concentration of Ni, Fe, and Mo metals of the recycled 1MNIF sample in the solution after the 5th photo Fenton degradation cycle was investigated using Inductively coupled plasma-mass spectrometry (ICP-MS). The percentage concentrations of leached metal ions in the solution were Ni (0.98%), Fe (0.45%), and Mo (0.008%), respectively. The minor leaching of metal ions during the reuse of the 1MNIF sample results in a slight decrease of photo-Fenton activity of 1MNIF after five cycles.

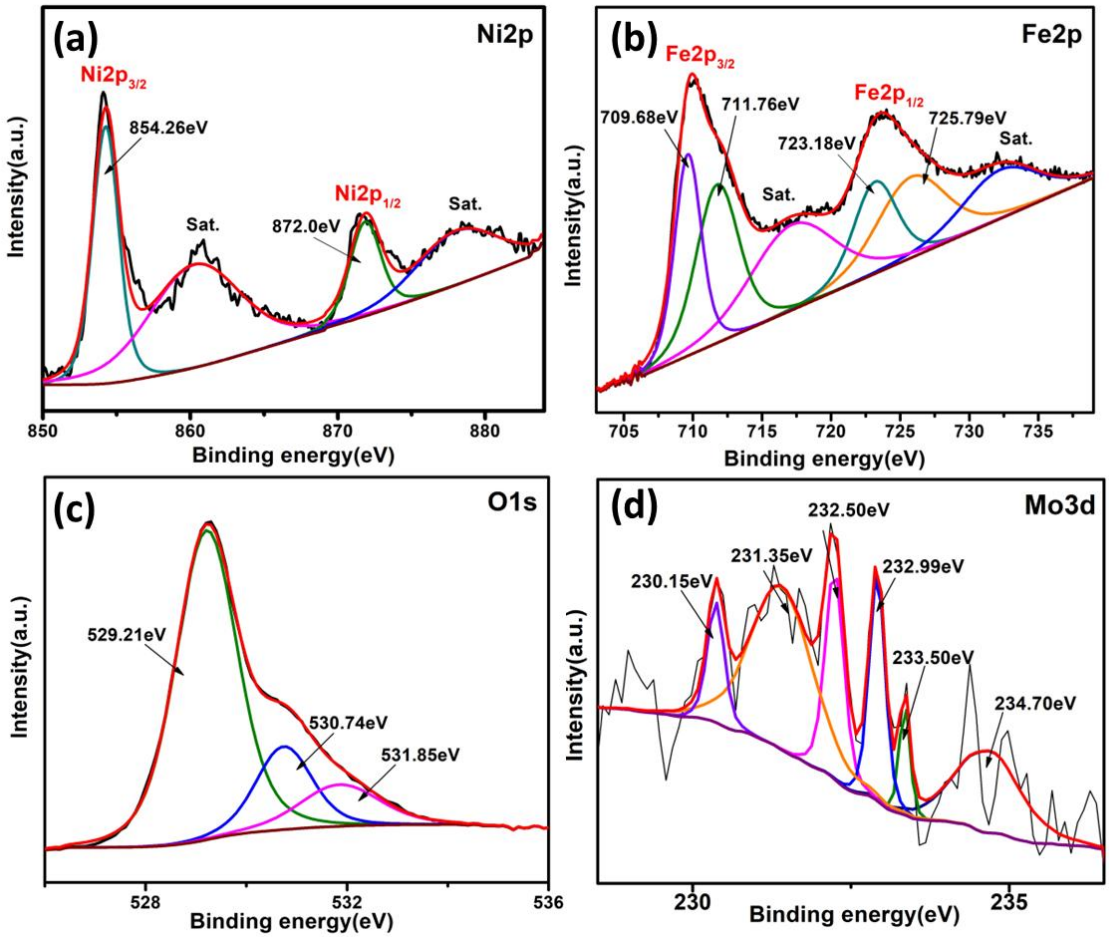


**Figure 6.6.** (a) Ni2p, (b) Fe2p, (c) O1s, and (d) Mo3d regions of the high-resolution XPS spectra of recycled 1MNIF sample.

XPS analysis was also done on the recycled 1MNIF sample (Fig. 6.6). Figure 6.6a displays two spin-orbit doublet peaks at 854.26 ($Ni2p_{3/2}$) and 872.0 eV ($Ni2p_{1/2}$) binding energies, indicating $Ni^{2+}$ in octahedral sites. Similarly, Fig. 6.6b shows two spin-orbit doublet peaks ($Fe2p_{3/2}$ and $Fe2p_{1/2}$) and two satellite peaks in the fitted Fe2p XPS spectrum. Further deconvolution confirmed the presence of $Fe^{3+}$ in both octahedral and tetrahedral sites. Figure 6.6c represents the O1s spectrum region. The three deconvoluted peaks obtained were similar to the fresh 1MNIF sample. These peaks indicate the presence of lattice oxygen (or metal-oxygen), oxygen vacancy, and chemisorbed oxygen species. A comparison of the XPS spectra of fresh and recycled 1MNIF samples (Fig. 5.7 and Fig. 6.6) shows no significant change in Ni2p, Fe2p, and O1s spectrum regions. Figure 6.6

shows deconvoluted Mo $3d_{5/2}$ peaks at 230.15 eV, 231.35 eV, and 232.50 eV due to Mo in the +4, +5, and +6 oxidation states. The Mo $3d_{3/2}$ peaks at 232.99 eV, 233.50 eV, and 234.70 eV are also due to Mo in the +4, +5, and +6 states in the recycled 1MNIF sample. Notably, the generation of $Mo^{4+}$ after the fifth consecutive cycle of photo-Fenton TC degradation is likely due to the reduction of $Mo^{6+}/Mo^{5+}$ by photogenerated electrons and oxygen vacancies.

### 6.3.3 DFT calculation results

As discussed in the introduction, for a photo-Fenton catalyst to be effective, its photo-excited nucleophilic sites must interact favorably with $H_2O_2$ to facilitate the production of ·OH radicals. Therefore, the positions of the HOMO and LUMO play a crucial role in determining the photo-Fenton activity of the catalyst. The HOMO and LUMO indicate the nucleophilic and electrophilic sites on the photocatalyst, respectively. In this context, the ground-state HOMO and LUMO positions reveal the nucleophilic and electrophilic sites before photoexcitation, while the excited-state HOMO and LUMO positions indicate these sites after photoexcitation. Figure 6.7a shows the ground-state HOMO and LUMO distributions in the MoNIF33 cluster. The HOMO is primarily located on Ni(Oct) and Fe(Oct), whereas the LUMO is partially distributed over Fe(Oct), Fe(Td), and Mo(Oct).

Next, single-point TD-DFT calculation was carried out on the optimized MoNIF33 cluster. Figure 6.8 displays the MoNIF33 cluster's simulated absorption spectra obtained from TD-DFT calculation. The vertical lines depict the excitations associated with electronic transitions at different wavelengths. The solid black curve in the figure displays the experimental solid-state UV-visible spectrum of the MoNIF33 cluster. The excited state HOMO-LUMO analysis was implemented on the oscillator frequency corresponding to the

552 nm (Figure 6.8) excited state. In the photo excited state, HOMO shifted from Ni(Oct), Fe(Oct) to Fe(Td) and lattice oxygens adjacent to the Mo metal centre (Fig. 6.7b).

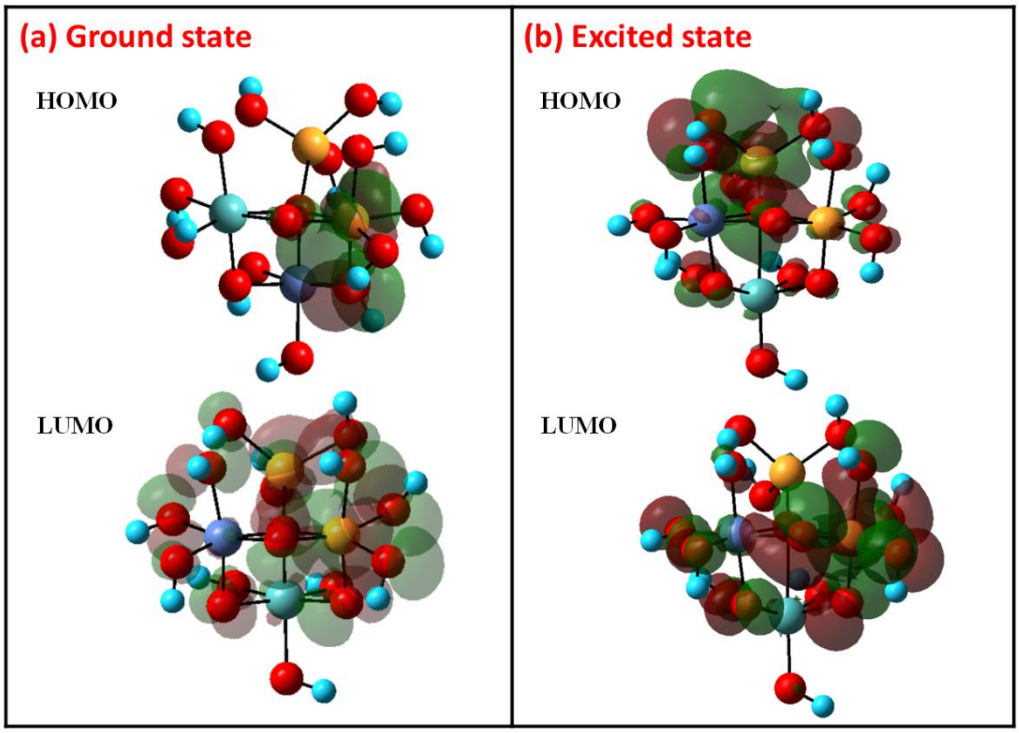


**Figure 6.7** The calculated HOMO/LUMO (a) ground state, and (b) excited state (552 nm) using DFT and TDDFT methods.

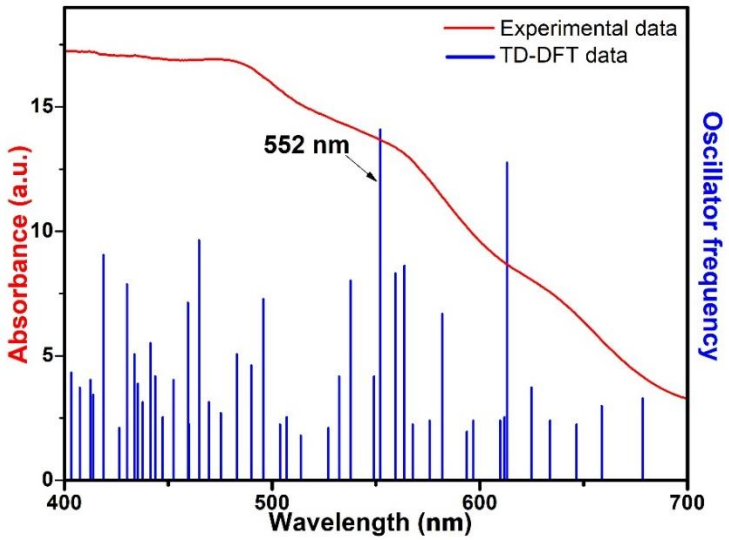


**Figure 6.8** Solid-state UV-visible reflectance spectrum of 1MNIF (solid red curve) and TD-DFT calculated UV-visible absorption spectrum of MoNIF33 cluster model (blue).

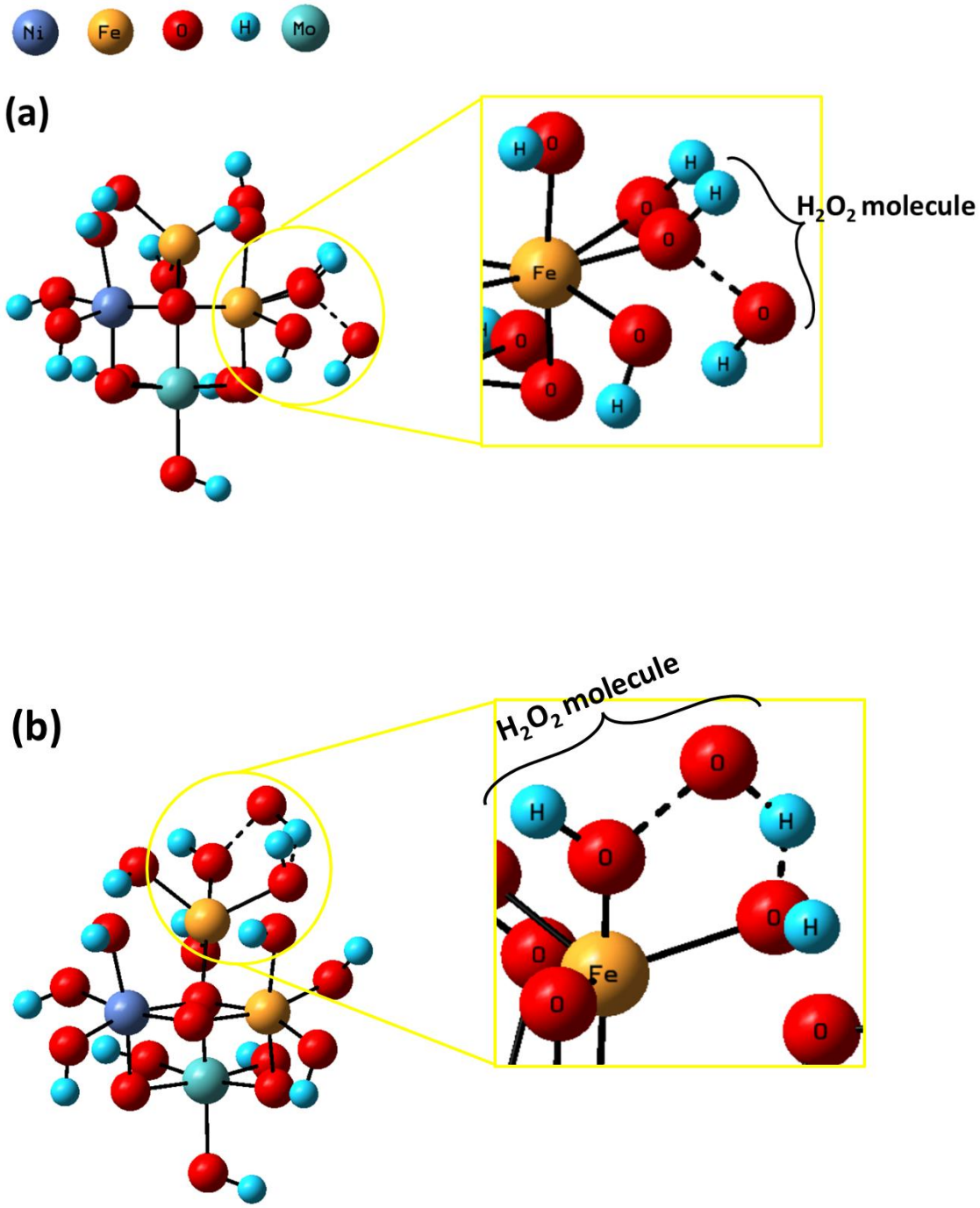


**Figure 6.9** The optimized structure of (a) $H_2O_2$_Fe(Oct)_MoNIF33_GS, and (b) $H_2O_2$_Fe(Td)_MoNIF33_ES systems.

After this, DFT calculations were conducted to investigate the interaction of $H_2O_2$ with the Mo-doped $NiFe_2O_4$ (MoNIF33) cluster in the ground state and excited state. It was found that $H_2O_2$ interacts best with the octahedral Fe position when MoNIF33 is in its

ground state. In contrast, $H_2O_2$ gives the lowest interaction energy with the tetrahedral Fe position (excited state HOMO location) when MoNIF33 is in the photoexcited state. The optimized $H_2O_2$ interaction structures are abbreviated as $H_2O_2$_Fe(Oct)_MoNIF33_GS (*$H_2O_2$ interacts with Fe(Oct) of MoNIF33 cluster in the ground state*) and $H_2O_2$_Fe(Td)_MoNIF33_ES (*$H_2O_2$ interacts with Fe(Td) of MoNIF33 cluster in excited state*) in the rest of the chapter (Figures 6.9a and 6.9b). The interaction potential energies of $H_2O_2$_Fe(Oct)_MoNIF33_GS and H2O2_Fe(Td)_MoNIF33_ES systems have been calculated using equations 6.4 and 6.5.

$$E_{interaction} = E_{(H2O2\_Fe(Oct)\_MoNIF33\_GS)} - [\, E_{(MoNIF33)} + E_{(H2O2)}] \quad (6.4)$$

$$E_{interaction} = E_{(H2O2\_Fe(Td)\_MoNIF33\_ES)} - [\, E_{(MoNIF33)} + E_{(H2O2)}] \quad (6.5)$$

In equations 6.4 and 6.5, 'E' represents the calculated potential energy of the respective molecular system.

**Table 6.2** The calculated potential energy for different molecules and systems. (1 Hartree = 27.21eV)

| **System** | **Potential energy (Hartree)** | **Interaction energy (Hartree)** |
|---|---|---|
| $H_2O_2$ | -151.572 | |
| MoNIF33 | -9223.189 | |
| $H_2O_2$_Fe(Oct)_MoNIF33_GS | -9374.673 | 0.0881 |
| $H_2O_2$_Fe(Td)_MoNIF33_ES | -9374.765 | -0.0053 |

Table 6.2 presents the potential energies of $H_2O_2$ molecule, $H_2O_2$_Fe(Oct)_MoNIF33_GS, and $H_2O_2$_Fe(Td)_MoNIF33_ES systems. The interaction energies of the $H_2O_2$_Fe(Oct)_MoNIF33_GS and H2O2_Fe(Td)_MoNIF33_ES interaction models are 0.0881 and -0.0053 Hartree, respectively. Thus, the $H_2O_2$_Fe(Td)_MoNIF33_ES

interaction model demonstrates the most negative interaction energy. Hence, Mo doping in $NiFe_2O_4$ affects the interaction of $H_2O_2$ with MoNIF33 in the ground and photoexcited states. This phenomenon can be better understood by Natural bond orbital (NBO) analysis

Figures 6.10 (a-d) show the change in different bond lengths in $H_2O_2$_Fe(Oct)_MoNIF33_GS, and $H_2O_2$_Fe(Td)_MoNIF33_ES interaction systems. Figure 6.10c shows that the oxygen of $H_2O_2$ interacts with Fe(Oct) of the MoNIF33 system in the $H_2O_2$_Fe(Oct)_MoNIF33_GS model. Figure 6.10d shows that the oxygen of $H_2O_2$ interacts with Fe(Td), and the terminal hydrogen of $H_2O_2$ interacts with oxygen coordinated to Fe(Td) in $H_2O_2$_Fe(Td)_MoNIF33_ES system. The $O_\alpha$-$O_\beta$ bond length of $H_2O_2$ part in $H_2O_2$_Fe(Oct)_MoNIF33_GS, and $H_2O_2$_Fe(Td)_MoNIF33_ES systems is 1.686 Å, and 1.763Å. The longer or more weakened $O_\alpha$-$O_\beta$ bond of $H_2O_2$ signifies greater bond activation. Thus, $O_\alpha$-$O_\beta$ bond activation is substantially more in the $H_2O_2$_Fe(Td)_MoNIF33_ES interaction system, in line with this system's negative (or lower) interaction energy.

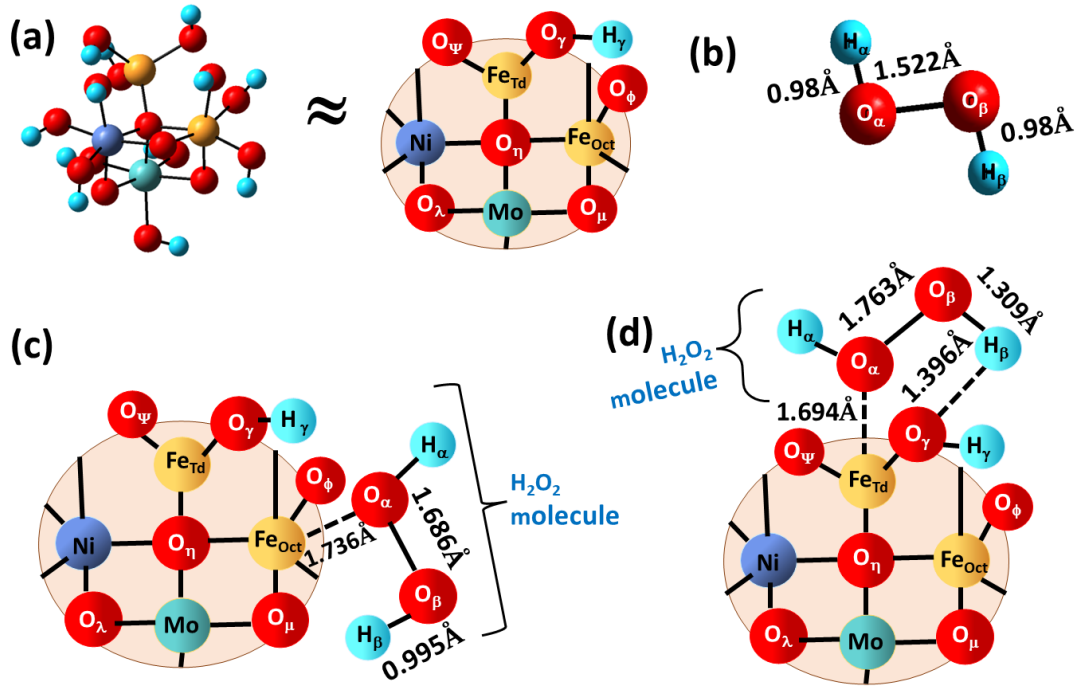

**Figure 6.10** (a) A 2-dimensional projection of the MoNIF33 model showing the abbreviations used for various atom types; (b) The optimized model of $H_2O_2$ molecule showing various bond lengths; (c) displays various interaction lengths in $H_2O_2$_Fe(Oct)_MoNIF33_GS, and (d) depicts various interaction lengths in the $H_2O_2$_Fe(Td)_MoNIF33_ES systems.

Natural bond orbital (NBO) calculations at the same level of theory (Table 6.2) as earlier were performed on optimized $H_2O_2$_Fe(Oct)_MoNIF33_GS, and $H_2O_2$_Fe(Td)_MoNIF33_ES conformations to calculate the second-order stabilization energy $E^{(2)}$ due to electron delocalization. The abbreviations for atom types in Fig. 6.10c and 6.10d systems have also been used to describe the NBO analysis results. The equation employs second-order perturbation theory to calculate this energy $E^{(2)}$ is given in previous chapter 5.[239]

**Table 6.3** The delocalization energy ($E^{(2)}$ in kcal/mol) analysis of charge transfer from donor to acceptor NBO of the $H_2O_2$_Fe(Oct)_MoNIF33_GS, and $H_2O_2$_Fe(Td)_MoNIF33_ES systems.

| System | Donor NBO | Acceptor NBO | $E^{(2)}$(kcal/mol) |
|---|---|---|---|
| $H_2O_2$_Fe(Oct)_MoNIF33_GS | LP ($Fe_{Oct}$) | BD*($O_\alpha$– $O_\beta$) | 0.52 |
| | BD($O_\alpha$ – $O_\beta$) | LP*($Fe_{Oct}$) | 4.51 |
| | BD($Fe_{Oct}$ - $O_\mu$) | LP*(Mo) | 24.67 |
| | LP(Mo) | BD*($Fe_{Oct}$ - $O_\mu$) | 3.08 |
| $H_2O_2$_Fe(Td)_MoNIF33_ES | LP ($Fe_{Td}$) | BD*($O_\alpha$ – $O_\beta$) | 17.38 |
| | BD($O_\alpha$ – $O_\beta$) | LP*($Fe_{Td}$) | 16.31 |
| | BD(Mo-$O_\eta$) | LP*($Fe_{Td}$) | 20.79 |
| | LP ($O_\gamma$) | BD*($H_\beta$-$O_\beta$) | 7.57 |

Table 6.3 shows the significantly larger charge transfers (or delocalization) in the $H_2O_2$_Fe(Td)_MoNIF33_ES system compared to the $H_2O_2$_Fe(Oct)_MoNIF33_GS

interaction system. The $H_2O_2$_Fe(Oct)_MoNIF33_GS system, displays a weak charge transfer from LP($Fe_{Oct}$) to BD*($O_\alpha$– $O_\beta$) with 0.52 kcal/mol interaction energy ($E^{(2)}$ value). Simultaneously, there is a reverse charge transfer from BD($O_\alpha$– $O_\beta$) to LP*($Fe_{Oct}$) with 4.51 kcal/mol $E^{(2)}$ value. These weak charge transfers cause only a slight activation of $O_\alpha$– $O_\beta$ bond of $H_2O_2$ molecule. In contrast, the BD ($Fe_{Oct}$ -$O_\mu$) charge transfer to the LP*(Mo) occurs with a considerably higher $E^{(2)}$ value i.e. 24.67 kcal/mol. On the contrary, the charge transfer from LP(Mo) to BD*($Fe_{Oct}$ - $O_\mu$) only has 3.08 kcal/mol $E^{(2)}$ value.

In $H_2O_2$_Fe(Td)_MoNIF33_ES system, charge transfer takes place from LP ($Fe_{Td}$) to BD*($O_\alpha$ – $O_\beta$) with 17.38 kcal/mol delocalization energy. Concurrently, a back donation occurs from BD($O_\alpha$ – $O_\beta$) to LP*( $Fe_{Td}$) with 16.31 kcal/mol $E^{(2)}$ value. Both charge transfers are the reasons for the significantly increased weakening and activation of the $O_\alpha$ – $O_\beta$ bond of $H_2O_2$ molecule in the photoexcited state. On the other hand, charge transfer occurs from BD(Mo-$O_\eta$) to LP*($Fe_{Td}$) with 20.79 kcal/mol $E^{(2)}$ value. This charge transfer promotes the earlier two charge transfers between $Fe^{(2)}$ and $O_\alpha$ – $O_\beta$ related NBOs. Complementary to this, another charge transfer takes place from LP ($O_\gamma$) to BD*($H_\beta$-$O_\beta$) with 7.57 kcal/mol interaction energy. Hence, the delocalization in the $H_2O_2$_Fe(Td)_MoNIF33_ES system is considerably larger. Consequently, the bond activation of $O_\alpha$ – $O_\beta$ bond of $H_2O_2$ molecule is more in photoexcited state than in ground state, which leads to the efficient formation of OH• radicals during the photocatalytic reaction.

### 6.3.4 Photo-Fenton degradation mechanism

Figure 6.11 illustrates the proposed mechanism for the photo-Fenton degradation of TC by the Mo-doped $NiFe_2O_4$ photocatalyst. Experimental results from UV-DRS and Mott-Schottky analysis revealed that Mo doping reduced the band gap and shifted the VB and

CB band edges to higher (or more positive) values. Among all the doped samples, the 1% Mo-doped $NiFe_2O_4$ exhibited the best photo-Fenton activity, attributed to its lowest charge transfer resistance and highest charge separation efficiency, as confirmed by the Nyquist plot. The 1MNIF sample exhibits negligible dark Fenton degradation of TC. Contrary to this, the 1MNIF particles show high visible light photo-Fenton TC degradation activity.

DFT studies reveal that HOMO in the MoNIF33 (a cluster model of 1MNIF) system shifts from Fe(Oct) in the ground state to Fe(Td) in the photoexcited state. TDDFT calculations indicate that the excited state HOMO is localized on the Fe(Td) center. Effectively, the $Fe^{3+}$ occupying the Td site in 1MNIF is reduced to $Fe^{2+}$ by the photoexcited electrons. $H_2O_2$ interacts more effectively with the photoexcited model through the Fe(Td) site causing greater activation of its O-O bond and OH• radical generation. Scavenger experiments confirm that OH• radicals are the active species responsible for the photo-Fenton activity. These OH• radicals and photogenerated holes subsequently react with tetracycline (TC), oxidizing it into smaller aliphatic fragments (Equations 6.11, 6.12, and 6.13).

Overall, suitable visible light irradiation photo generates electron/hole pairs in the photocatalyst (equation 6.6). The photoexcited electrons can reduce $Fe^{3+}$ to $Fe^{2+}$ on the surface of the photocatalyst (Equation 6.7). Because the redox potential of $Mo^{6+}/Mo^{5+}$ is approximately 0.4 eV[231,255], the Mo dopant energy level just below the CB of 1MNIF can trap photogenerated carriers, enhancing charge separation and prolonging the charge carrier lifetimes (equation 6.8). Once $Mo^{6+}$ captures electrons, it is reduced to $Mo^{5+}$, forming a redox-active species capable of further reactions. $Mo^{5+}$ then interacts with $H_2O_2$ and facilitates the decomposition of $H_2O_2$ into •OH. Through this reaction, $Mo^{5+}$ is oxidized back to $Mo^{6+}$, ensuring the continuous regeneration of active sites and maintaining the catalytic cycle. The detection of $Mo^{4+}$ in the Mo3d XPS of recycled 1MNIF sample further

implies a redox cycle involving Mo in +6, +5, and +4 oxidation states, potentially contributing to enhanced catalytic performance. The dopant level electrons can also get photoexcited to convert $Fe^{3+}$ to $Fe^{2+}$ in the 1MNIF photocatalyst (equation 6.9). The latter interacts and reduces $H_2O_2$ to generate •OH radicals (Equations 6.10, and 6.11).

$$1MNFO + hv \rightarrow 1MNFO(e_{cb}^{-} + h_{vb}^{+}) \quad (6.6)$$

$$Fe^{3+} + e_{cb}^{-} \rightarrow Fe^{2+} \quad (6.7)$$

$$Mo^{6+}/Mo^{5+} + e_{cb}^{-} \rightarrow Mo^{5+}/Mo^{4+} \quad (6.8)$$

$$Mo^{5+}/Mo^{4+} + Fe^{3+} \rightarrow Fe^{2+} + Mo^{6+}/Mo^{5+} \quad (6.9)$$

$$e^{-} + H_2O_2 \rightarrow \bullet OH + OH^{-} \quad (6.10)$$

$$Fe^{2+} + H_2O_2 \rightarrow Fe^{3+} + \bullet OH + OH^{-} \quad (6.11)$$

$$\bullet OH + tetracyline \rightarrow TC\ fragments/CO_2 + H_2O \quad (6.12)$$

$$h^{+} + TC\ fragments \rightarrow CO_2 + H_2O \quad (6.13)$$

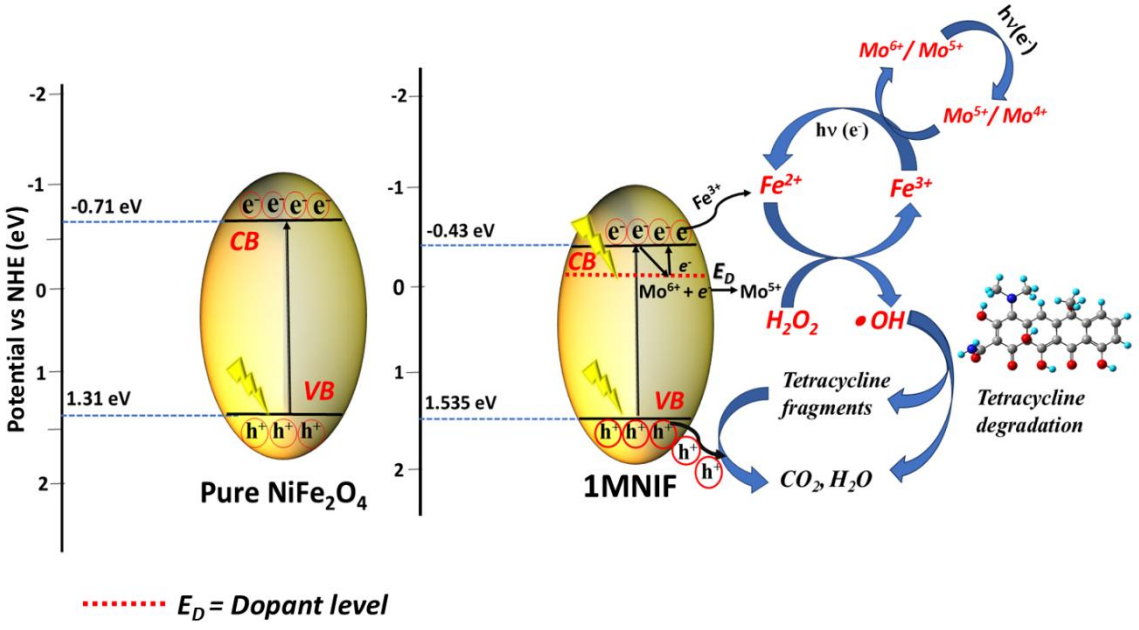


**Figure 6.11** Plausible mechanism for photo-Fenton degradation of TC by 1MNIF photocatalyst.

## 6.4 Conclusions

The spinel superparamagnetic $NiFe_2O_4$ semiconductor is a potential candidate for photo-Fenton degradation of organic pollutants due to its visible light band gap, photochemical stability, and magnetic separability. However, it suffers from low surface reaction rates, rapid electron-hole recombination, and poor visible light absorption. Mo doping addresses these limitations by enhancing charge separation and reducing charge recombination by introducing dopant levels in the band structures. Mo-doped $NiFe_2O_4$ photocatalysts were synthesized by a one-step hydrothermal method. A comparison of the Nyquist plots of the investigated samples shows that the 1% Mo-doped $NiFe_2O_4$ sample has the best charge transfer kinetics. The 1% Mo-doped $NiFe_2O_4$ demonstrated excellent photo-Fenton degradation of tetracycline, with appropriate recyclability. The TOF value of 1% Mo-doped $NiFe_2O_4$ photocatalyst is higher than other doped semiconductor photocatalysts previously reported.

Mo-doped $NiFe_2O_4$ has a reduced band gap (and the shifting of its band edges) show that the dopant Mo acts both as an electron trapper and supplier, improving charge separation and carrier lifetimes during the photo-Fenton process. DFT and TDDFT studies reveal that in the Mo-doped $NiFe_2O_4$ (MoNIF33) system, the HOMO shifts from Fe(Oct) in the ground state to Fe(Td) in the excited state. Additionally, Fe(Td) of Mo doped $NiFe_2O_4$ activates the O–O bond of $H_2O_2$ more effectively in the excited state, producing hydroxyl radicals. DFT and experimental results enable us to propose an effective mechanism for photo-Fenton TC degradation.